Applied Catalysis B: Environment and Energy 358 (2024) 124334

Contents lists available at ScienceDirect

Applied Catalysis B: Environment and Energy

journal homepage: www.elsevier.com/locate/apcatb

Spatial segregation of three-dimensional Al_2O_3 supported PtSn catalyst for improved sintering-resistant at high temperature

Zhun Zhang [a,b,1], Congcong Du [a,1], Haowen Li [c,1], Jianyu Hu [d], Fan Yang [a,b], Jianyu Huang [e], Sulei Hu [d], Wei-Xue Li [c,*], Haifeng Xiong [a,b,**]

[a] State Key Laboratory of Physical Chemistry of Solid Surfaces, College of Chemistry and Chemical Engineering, Xiamen University, Xiamen 361005, China
[b] Innovation Laboratory for Sciences and Technologies of Energy Materials of Fujian Province (IKKEM), Xiamen 361102, China
[c] Department of Chemical Physics School of Chemistry and Materials Science, University of Science and Technology of China, Hefei, Anhui 230026, China
[d] Hefei National Laboratory for Physical Science at the Microscale, University of Science and Technology of China, Hefei, Anhui 230026, China
[e] Clean Nano Energy Center, State Key Laboratory of Metastable Materials Science and Technology, Yanshan University, Qinhuangdao 066004, China

ARTICLE INFO

Keywords:
PtSn catalyst
Flower-shaped Al_2O_3
Direct propane dehydrogenation
Deactivation and regeneration
In-situ/Operando TEM

ABSTRACT

Many catalytic reactions operate within high-temperature environment, inevitably leading to the sintering of small nanoparticles. Consequently, the design of sintering-resistant metal nanocatalysts at elevated temperatures pose significant challenges. Herein, we introduce an approach, employing a 3D flower-shaped Al_2O_3 (F-Al_2O_3), to stabilize nanoparticles by establishing a spatial separation in propane dehydrogenation (PDH). The PDH reaction conducted is just a test system at non-relevant conditions. Both *ex-situ* and *in-situ* TEM analyses evidence that PtSn nanoparticles on the F-Al_2O_3 exhibit remarkable resistance to sintering under high-temperature oxidative and reductive conditions. The propane conversion of PtSn/F- Al_2O_3 fully rebounds to its initial state and the average particle diameter of PtSn/F- Al_2O_3 remains virtually unchanged after seven PDH cycles. In contrast, 2D Al_2O_3 nanosheets (C-Al_2O_3) experience severe PtSn nanoparticle sintering. Computational studies highlight the effectiveness of the 3D flower-shaped Al_2O_3 in obstructing particle migration and ripen through spatial segregation. This strategy involving the construction of three-dimensional space support presents a promising avenue for the design of sintering-resistant nanocatalysts.

1. Introduction

Propylene is one of the most important chemical monomers for producing valuable chemicals in industry [1–3]. The propane direct dehydrogenation (PDH) *via* heterogeneous catalysts provides the facile route to produce propylene with high selectivity [4,5]. Pt-based catalysts are preferred for the PDH because of the high activity and selectivity resulted from the strong ability of C−H bond rupture and poor ability for C−C bond cleavage [6]. On the other hand, PDH reaction is a thermodynamically limited and strong endothermic reaction [7,8] and therefore high reaction temperature (>500°C) is critical in order to achieve the decent propane conversion [9–12]. However, at high reaction temperatures, Pt nanoparticles are prone to grow and sinter in PDH, which were reported in many previous works [13–15]. Moreover, because of the participation of hydrocarbons, coke is formed during the PDH, which is partly the cause of the catalyst deactivation [16,17].

To regenerate the deactivated Pt catalysts, aftertreatments such as oxidation, reduction or adding halogens (such as, Cl_2, HCl, CCl_4, or F_2) are used to treat the spent Pt-containing catalyst at elevated temperature so that the coking can be removed or small Pt particle size in the initial catalyst can be restored [18]. In this regard, alumina-supported Pt nanocatalyst loses activity during PDH reaction with coke formation, and the strategies of oxidation/reduction were used for the regeneration [19]. In our previous work, a spent Pt/CeO_2 single-atom catalyst after PDH was treated in oxidizing condition to remove the coking and to restore the singly dispersion of Pt [18]. However, the time-resolved evolution of Pt particles over the Pt catalyst during the aftertreatment remain unclear [20–24].

* Corresponding author.
** Corresponding author at: State Key Laboratory of Physical Chemistry of Solid Surfaces, College of Chemistry and Chemical Engineering, Xiamen University, Xiamen 361005, China.
E-mail addresses: wxli70@ustc.edu.cn (W.-X. Li), haifengxiong@xmu.edu.cn (H. Xiong).
[1] These authors contributed equally to this work.

https://doi.org/10.1016/j.apcatb.2024.124334
Received 28 February 2024; Received in revised form 30 May 2024; Accepted 23 June 2024
Available online 26 June 2024

In PDH reaction, an industrially practical Pt catalyst contains Pt and promoters such as Sn or Ga [25–29]. The existence of promoters helps improving the propylene selectivity of Pt catalysts [30–32]. For the Pt catalysts in PDH, Al_2O_3 is the most commonly used carrier [5,33,34]. Previous works found that the textural properties of alumina support, such as morphology and surface area, can significantly affect the sintering of metal particles and further affect its catalytic performance in catalysis [4,35]. For example, nanosheet-assembled γ-Al_2O_3 (NA-Al_2O_3) architectures can stabilize ultrafine palladium active phases in methane oxidation [35]. Therefore, it is plausible that nanostructure alumina can stabilize the Pt-containing nanoparticles over Pt catalysts in PDH reaction and the relative regeneration.

In this study, to investigate the catalyst evolution during regeneration and to investigate the effect of support morphology on the particle sintering over the Pt catalysts in PDH, we synthesize a three-dimensional (3D) flower-shaped Al_2O_3 (F-Al_2O_3) to load PtSn nanoparticles by constructing a 3D spatial distance through a compartmentalized strategy. For the purpose of comparison, PtSn catalysts supported on a commercial two-dimensional (2D) Al_2O_3 nanosheet and α-Al_2O_3 were also prepared (Scheme 1). Both *ex-situ* and *in-situ* TEM techniques were used to characterize the catalysts during regeneration under both high-temperature oxidative and reductive atmospheres. The sintering behavior of PtSn nanoparticles on various Al_2O_3 supports was also investigated using theoretical simulations. Factors such as the contact angle of the supported metal nanoparticles and specific surface area of supports were analyzed to elucidate the sintering patterns observed.

2. Experimental section

2.1. Synthesis of flower-shaped Al_2O_3 (F-Al_2O_3)

The synthesis of flower-shaped Al_2O_3 was based on a modified method reported in previous work [35]. Firstly, 1.51 g of Al $(NO_3)_3{\cdot}9\ H_2O$, 0.70 g of K_2SO_4 and 0.50 g of $CO(NH_2)_2$ were mixed and dissolved in 80 mL deionized water. Then, the mixed solution was transferred into a 200 mL Teflon-lined stainless steel autoclave. After heating in an oven at 180°C for 3 h, the autoclave was cooled down to room temperature and washed, followed by filtration for several times with deionized water. Then, the obtained white precipitate was collected and dried overnight at 80 °C in oven. Finally, the precipitate was calcined at 500°C in a muffle furnace with a ramping rate of 1 °C/min and kept at 500°C for 2 h.

2.2. Synthesis of PtSn/F-Al_2O_3, PtSn/C-Al_2O_3, PtSn/α-Al_2O_3 and PtSn/C-Al_2O_3-1150

0.5 wt% Pt and 0.8 wt% Sn were loaded on F-Al_2O_3 by incipient wetness co-impregnation method with ethanol as solvent and $Pt(NO_3)_2$ and $SnCl_2{\cdot}2\ H_2O$ as metal precursors. The obtained samples were dried overnight at 80 °C after the impregnation. Finally, the samples were calcined at 500°C in a muffle furnace with a ramping rate of 1 °C/min and then kept at 500°C for 4 h. The resulting sample was named PtSn/F-Al_2O_3. The preparation of the PtSn/C-Al_2O_3 and PtSn/α-Al_2O_3 followed the same approach as PtSn/F-Al_2O_3, except that C-Al_2O_3 (Macklin, γ-Al_2O_3, 20 nm) and α-Al_2O_3 (Macklin, 500 nm) were commercially available supports and used as received. In comparison, C-Al_2O_3 was calcined at 1150°C in a muffle furnace with a ramping rate of 10 °C/min and kept at 1150°C for 4 h, which was denoted as C-Al_2O_3-1150. Then PtSn/C-Al_2O_3-1150 was synthesized using the same process as PtSn/F-Al_2O_3.

2.3. Catalyst characterization

The as-prepared fresh (reduction at 600°C for 2 h before PDH reaction) and spent (after 7 PDH cycles) catalysts were subjected to a range of characterizations. The elemental compositions were measured by inductively coupled plasma-optical emission spectroscopy (ICP-OES, Agilent 5110, USA). The powder X-Ray diffraction (XRD) patterns were recorded using a Rigaku SmartLab Powder Diffractometer (XRD, SmartLab SE, Japan, HyPix-400 detector, sealed tube, Cu Kα radiation with Ni β-filter). Scanning electron microscopy (SEM, Hitachi S-4800, Japan) images were taken on a Hitachi S-4800 electron microscope to visualize the morphologies of different Al_2O_3 supports. Transmission electron microscopy (TEM) images and high-angle annular-dark-field (HAADF) scanning transmission electron micrographs (STEM, Tecnai F30, Netherlands) were acquired using a Tecnai F30 transmission electron microscope operated at 200 kV. N_2 adsorption/desorption isotherms were carried out in the Micromeritics ASAP 2020 (USA) at 77 K. The specific surface areas of the samples were calculated by Brunauer-Emmett-Teller (BET) method. The Pt species were identified by CO diffuse reflectance infrared spectroscopy (DRIFTS) in a Thermo Scientific Nicolet iS50 FTIR spectrometer equipped with a Harrick Praying Mantis high-temperature reaction chamber (ZnSe windows). In a typical run, fresh samples were packed into an *in-situ* cell, and He was introduced to the chamber for pretreatment at 200 °C with a ramping rate of 10 °C min^{-1} and then kept for 1 h. After the sample was cooled to 27 °C, CO diffuse reflectance infrared spectroscopy was performed and the spectra were recorded. For the spent catalysts, the coke was firstly removed at 450°C in air with a ramping rate of 10 °C min^{-1} and remained for 1 h. The characterization condition was the same as the fresh catalysts. *In-situ* TEM experiments were performed in an environmental electron microscopy (FEI Titan G2 80–300 kV) with spherical aberration correction at 300 kV. First, a flowing O_2 gas (purity = 99.999 %) at the pressure of 0.2 mbar was inserted into the TEM chamber through a variable pressure leak valve and then the temperature of the heated area of the chip was raised to 500 °C at a rate of 10 °C/s. After the heating is stable, O_2 was evacuated from the electron microscope chamber and then H_2 gas was immediately introduced at the pressure of 0.2 mbar and T=600 °C for approximately 30 min. To overcome any potential e-beam effects (*i.e.*, to rule them out as factors affecting the *in-situ* TEM results and to ensure that we have studied the intrinsic behavior of nanoparticles), we employed a camera (Oneview)

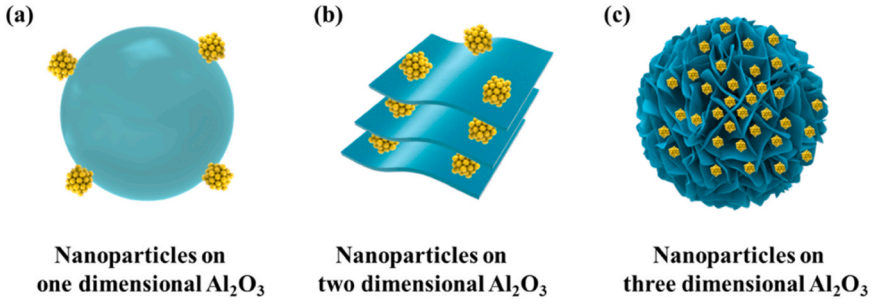

Scheme 1. Structural illustration of PtSn nanoparticles supported on alumina supports with different architectures. (a) PtSn nanoparticles supported on one-dimensional Al_2O_3. (b) PtSn nanoparticles supported on two-dimensional Al_2O_3. (c) PtSn nanoparticles supported on three-dimensional Al_2O_3.

to collect a series of *in-situ* images under the condition of beam blank. TEM chips (FEI) based on MEMS through holes were used in all the *in-situ* TEM heating experiments.

2.4. Direct dehydrogenation of propane

Direct dehydrogenation of propane. At atmosphere pressure, the performance of catalysts was tested in a quartz fixed-bed reactor with 6 mm inner diameter and 47 cm length. In a typical process, 250 mg

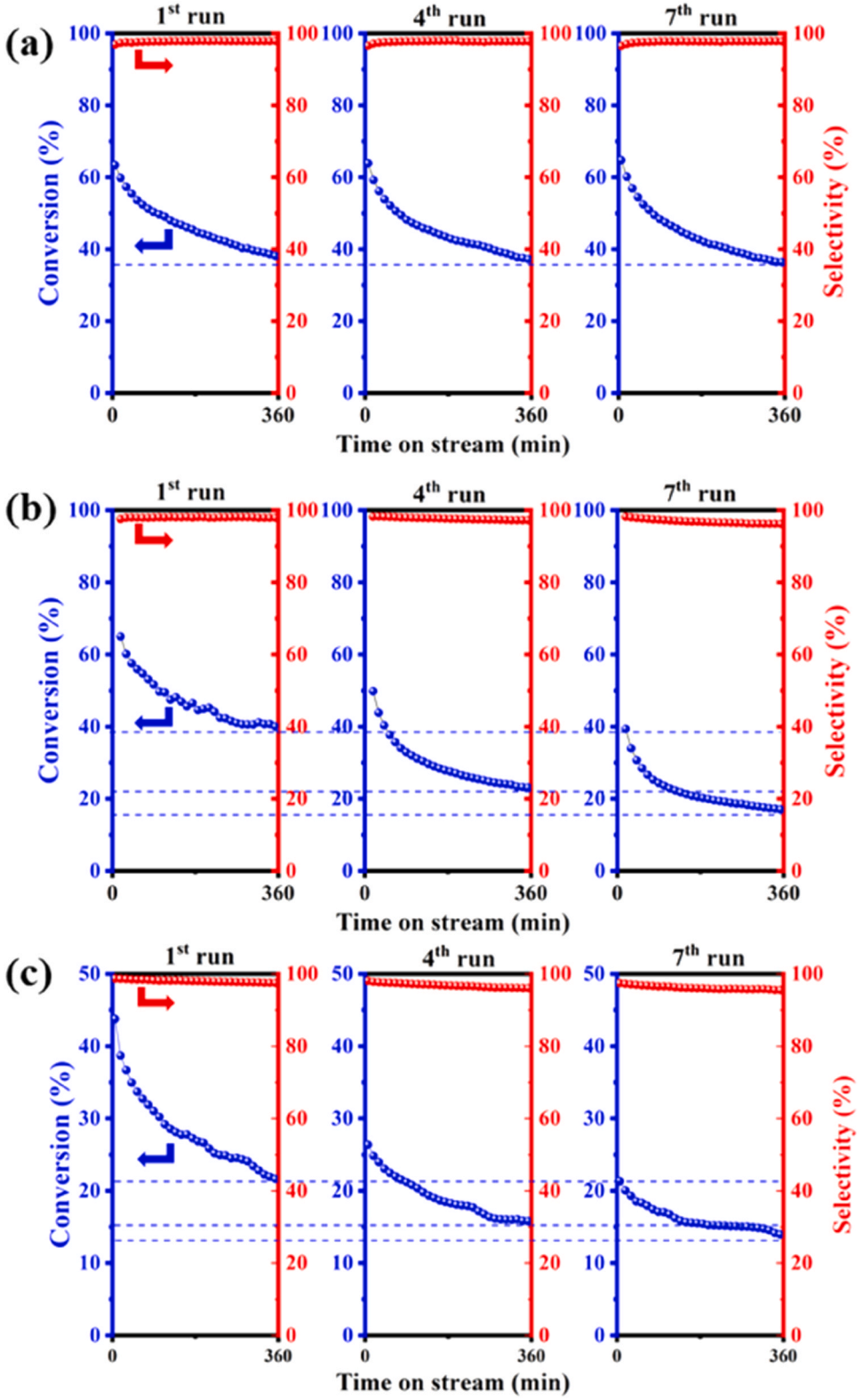

Fig. 1. Catalytic performances of different catalysts. (a) PtSn/F-Al_2O_3 (0.25 g catalyst, 600℃, 101 kPa, $C_3H_8/H_2/He$=4/4/19 mL min^{-1}, WHSV = 589.2 h^{-1}). (b) PtSn/C-Al_2O_3 (same conditions as (a)). (c) PtSn/α-Al_2O_3 (1.0 g catalyst, 600℃, 101 kPa, $C_3H_8/H_2/He$=2/2/23 mL min^{-1}, WHSV = 73.6 h^{-1}).

catalyst with particle diameter of 40–60 mesh was packed inside the quartz tubular reactor. The sample was first heated to 600 °C with a ramping rate of 10 °C min^{-1} and retained at 600 °C for 2 h in the flowing H_2 (20 mL min^{-1}). Afterward, a mixture of C_3H_8, H_2 and He (4: 4: 19) was fed at a rate of 27 mL min^{-1}. The gas products were analyzed by an online GC 2060 equipped with a flame ionization detector. The propane conversion, selectivity to propylene and carbon balance were calculated from the following three equations, respectively:

$$\text{Conversion}(\%) = 100 \times \frac{[C_3H_8]_{in} - [C_3H_8]_{out}}{[C_3H_8]_{in}}$$

$$\text{Selectivity}(\%) = 100 \times \frac{[C_3H_6]_{out}}{[C_3H_8]_{in} - [C_3H_8]_{out}}$$

$$\text{Carbon balance}(\%) = 100 \times \frac{[CH_4]_{out} + 2\times[C_2H_6]_{out} + 2\times[C_2H_4]_{out} + 3\times[C_3H_8]_{out} + 3\times[C_3H_6]_{out}}{3\times[C_3H_8]_{in}}$$

Where $[C_3H_8]$, $[C_3H_6]$, $[C_2H_6]$, $[C_2H_4]$ and $[CH_4]$ means the corrected integrated peak area of propane, propylene, ethane, ethylene and methane, respectively. And "in" and "out" means the feed gases and products, respectively.

2.5. Catalyst regeneration process

After the PDH reaction, the spent PtSn catalyst was cooled down to room temperature under the flowing He (19 mL min^{-1}). Then, the catalyst was calcined at 550 °C for 1 h in flowing 20 % O_2/He (20 mL min^{-1}) with a ramping rate of 10 °C min^{-1} and then cooled down to room temperature. Afterward, the catalyst was repeated for the PDH reaction using the same process.

2.6. Simulation methods

The contact angles of metal particles on various supports were determined by analyzing molecular dynamics (MD) simulation trajectory conducted under the LASP code [36]. The cohesive energy of metal nanoparticles was obtained from density functional theory (DFT) calculations performed using Vienna Ab Initio Simulation Package (VASP) code [37].

3. Result and discussion

3.1. Performances of catalysts in propane dehydrogenation

The catalytic performances of the different alumina supported PtSn catalysts were evaluated in a quartz fixed-bed reactor at 600°C. Detailed experimental conditions were found in the experimental section. The catalytic results of all catalysts (C_3H_8 conversion and C_3H_6 selectivity) are shown in Fig. 1, Fig. S1 and Fig. S2. For each catalyst, a regeneration process including an oxidation step and a reduction step was adopted to reactivate the catalyst. The oxidation step was used to remove the coke and a reduction step was used to reduce the metal. In seven PDH runs, PtSn/F-Al_2O_3 catalyst (Fig. 1a) did not show deactivation during multiple regeneration cycles. Meanwhile, the propylene selectivity is stable at 99 %. At 500 °C, PtSn/F-Al_2O_3 exhibited outstanding long-term stability (Fig. S1) and the catalyst exhibited the stable conversion of 18 % with ~100 % propylene selectivity without any drop in 720 min run.

In contrast, the PtSn/C-Al_2O_3 (Fig. 1b) underwent severe permanent deactivation during regeneration at 600 °C and a regeneration process (oxidation and reduction) cannot recover the conversion to the initial state. Specifically, after 4 and 7 PDH cycles at 600 °C, the initial conversion dropped from 65.0 % to 49.8 % and 39.3 %, respectively. Moreover, the conversion after reaction for 6 h also dropped from 40.0 % to 23.1 % and 17.0 %, respectively, and the propylene selectivity after reaction of 6 h dropped from 97.9 % to 96.1 %. In addition, a commercial α-Al_2O_3 supported PtSn (PtSn/α-Al_2O_3) showed low initial conversion (Fig. 1c). By adjusting the space-time yield (589.2 h^{-1} to 73.6 h^{-1}), the initial conversion of PtSn/α-Al_2O_3 was controlled to the same level as the PtSn/C-Al_2O_3 catalyst for comparison. It can be seen that the permanent deactivation occurred during PDH and regeneration. After 4 and 7 PDH cycles, the initial propane conversion changed from 43.7 % to 26.3 % and 21.3 % respectively. After PDH reaction for 6 h for each cycle, the conversion changed from 21.3 % to 15.7 % and 13.7 % respectively. At the same time, the propylene selectivity also dropped from 98.7 % to 95.3 %. The poor catalytic performances of the PtSn catalyst supported on α-Al_2O_3 were also demonstrated by calcining C-Al_2O_3 nanosheet at 1150°C to form α-Al_2O_3, which was named the C-Al_2O_3-1150 (Fig. S3). The initial activity of the PtSn/C-Al_2O_3-1150 (Fig. S2) is as low as 4 % and it could not be increased by changing the space-time yield.

The catalytic performances of the PtSn catalysts above demonstrates that the morphology of the alumina support affects the catalytic reactivity and deactivation behavior. To reveal the deactivation behavior of the PtSn catalysts, we have performed the following *ex-situ* and *in-situ* characterizations for the fresh and spent PtSn/Al_2O_3 catalysts.

3.2. Sample ex-situ characterizations

3.2.1. Morphology of supports

The morphology of the flower-shaped Al_2O_3 (F-Al_2O_3), commercial Al_2O_3 nanosheets (C-Al_2O_3), commercial α-Al_2O_3 and C-Al_2O_3-1150 (C-Al_2O_3 calcined at 1150°C) was characterized by the SEM/TEM techniques (Fig. 2, Fig. S4 and Fig. S5). From the SEM of F-Al_2O_3 (Fig. 2a), it is seen that the flower-shaped Al_2O_3 and the cross-linked petal-like nanosheets were clearly visualized, indicating the successful synthesis of the support. The morphology of the F-Al_2O_3 is maintained after loading metals even going through 7 PDH cycles (Fig. S4a-b), indicating that the F-Al_2O_3 had excellent thermal durability. The TEM images of PtSn/F-Al_2O_3-Spent (Fig. S4c-d) catalysts further demonstrated that the petal-like nanosheets of the F-Al_2O_3 were intersecting and the unique architectures could effectively prevent the migration and sintering of nanoparticles by spatial segregation (compartmentalization).TEM image of the commercial C-Al_2O_3 (Fig. 2b) showed that the Al_2O_3 was nanosheet structure with width of ~20 nm and the nanosheets were partially stacked. The SEM image of α-Al_2O_3 (Fig. 2c) revealed the round shape of the α-Al_2O_3 and the edges of Al_2O_3 were connected each other and tightly packed. The specific surface area (S_{BET}) of the sphere-like morphology of α-Al_2O_3 is ~6 m^2 g^{-1} (Table 1), which indicated that the internal pore structure of α-Al_2O_3 was completely destroyed and it is a nonporous solid structure, which agrees with the SEM observation.

3.2.2. Textural properties of supports and the elemental composition of catalysts

Table 1 summarizes the specific surface areas (S_{BET}) of different Al_2O_3 supports. The S_{BET} of F-Al_2O_3 and C-Al_2O_3 was determined to be 122 m^2 g^{-1} and 107 m^2 g^{-1} respectively. Likewise, the surface areas of both α-Al_2O_3 and C-Al_2O_3-1150 (C- Al_2O_3 calcined at 1150°C) were low, only 6 m^2 g^{-1} and 4 m^2 g^{-1}, respectively. This indicates that the pore structures of the two latter Al_2O_3 supports were completely nonporous solid structures.

The Pt and Sn contents on the fresh and spent PtSn/F-Al_2O_3 and PtSn/C-Al_2O_3 were measured by ICP-OES (inductively coupled plasma-optical emission spectroscopy) and the analysis results are shown in Table 1. The calculated metal loadings of Pt and Sn are 0.5 wt% and 0.8 wt%, respectively. The measured contents of Pt and Sn were 0.47 wt % and 0.79 wt% for PtSn/F-Al_2O_3-Fresh, and 0.48 wt% and 0.78 wt% for PtSn/C-Al_2O_3-Fresh, respectively. The actual contents of Pt and Sn were slightly lower than the theoretical values, which may be caused by the partial loss in the process of catalyst preparation. After 7 PDH cycles, the contents of Pt and Sn for PtSn/F-Al_2O_3-Spent were 0.47 wt% and 0.78 wt%, 0.48 wt% and 0.76 wt% for PtSn/C-Al_2O_3-Spent, respectively. For PtSn/α-Al_2O_3, the content of Pt and Sn did not change after several cycles of regeneration, which were 0.47 wt% and 0.77 wt%, respectively. Therefore, the elemental composition of the catalysts was unchanged after several cycles of regeneration, indicating that there is no metal loss during the PDH and regeneration processes.

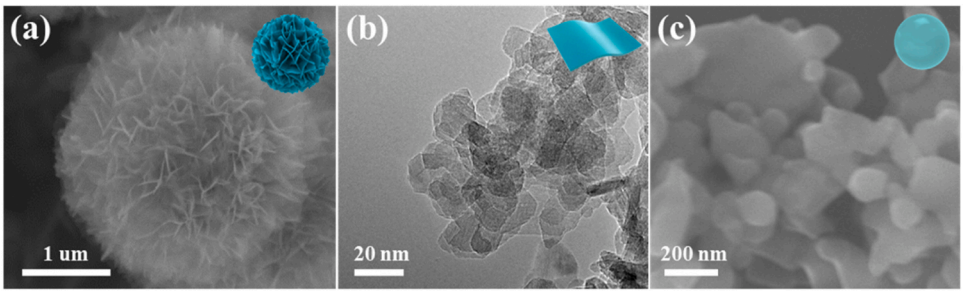

Fig. 2. SEM/TEM images showing the morphologies of different Al_2O_3 supports used for the PtSn catalysts. (a) SEM image of the as-synthesized flower-shaped alumina (F-Al_2O_3). (b) TEM image of alumina sheet (C-Al_2O_3). (c) SEM image of the commercial α-Al_2O_3. The insert in the upper right corner of each image is a sketch of the corresponding support.

Table 1
Textural properties of different Al_2O_3 supports and the elemental composition of the PtSn catalysts.

Supports	F-Al_2O_3	C-Al_2O_3	C-Al_2O_3-1150	α-Al_2O_3
Surface area (m^2 g^{-1})[a]	122	107	4	6
Catalysts	Elements	Theoretical value wt (%)		Actual value wt[b] (%)
PtSn/F-Al_2O_3-Fresh	Pt	0.50		0.47
	Sn	0.80		0.79
PtSn/F-Al_2O_3-Spent	Pt	0.50		0.47
	Sn	0.80		0.78
PtSn/C-Al_2O_3-Fresh	Pt	0.50		0.48
	Sn	0.80		0.78
PtSn/C-Al_2O_3-Spent	Pt	0.50		0.48
	Sn	0.80		0.76
PtSn/α-Al_2O_3-Fresh	Pt	0.50		0.47
	Sn	0.80		0.77
PtSn/α-Al_2O_3-Spent	Pt	0.50		0.47
	Sn	0.80		0.77

[a] Determined by the Brunauer-Emmett-Teller (BET) method.
[b] Determined by ICP-OES analysis.

3.2.3. XRD spectra

The XRD patterns of the fresh and spent PtSn catalysts before and after 7 cycles of PDH reaction are shown in Fig. 3. XRD patterns showed that there was no diffraction peak of metal Pt observed for fresh and spent PtSn/F-Al_2O_3, PtSn/α-Al_2O_3 (Fig. 3a) and PtSn/C-Al_2O_3 (Fig. 3b) catalysts, which may be due to the low Pt loading (0.5 wt%) or the highly dispersed Pt species. The small size of Pt species, such as single-atoms and/or clusters, will not present any diffraction peak of Pt in XRD patterns. However, the PtSn/C-Al_2O_3-1150-Fresh (Fig. 3b) had a distinct diffraction peak of Pt particle at 39.7 °, which resulted from the low specific surface area of C-Al_2O_3-1150 (4 m^2 g^{-1}, Table 1) and the large metal particle of PtSn/C-Al_2O_3-1150-Fresh (~32.0 nm, Fig. S6c). The XRD pattern of C-Al_2O_3-1150 showed that the crystal structure of C-Al_2O_3 had changed into α after calcined at 1150°C and its pattern was completely consistent with α-Al_2O_3 (Fig. S3). The low S_{BET} and SEM image (Fig. S5) of C-Al_2O_3-1150 showed that the nanosheet structure of C-Al_2O_3 was destroyed and presented the solid structure, which led to the large metal nanoparticles (~32.0 nm) when supported on C-Al_2O_3-1150. After 7 PDH cycles, the diffraction peak of Pt particle for PtSn/C-Al_2O_3-1150-Spent became sharper, which is attributed to the growth of the Pt particles after PDH reaction, showing the average metal particle diameter of ~38.0 nm (Fig. S6d).

3.2.4. HAADF-STEM images

To directly visualize the particle size before and after PDH, we performed HAADF-STEM for the samples. The HAADF-STEM images of the different catalysts before and after PDH are shown in Fig. 4 and Fig. S6. The average diameters are shown in Table 2. Fig. 4a showed that the average particle diameter of PtSn is 6.7±1.7 nm. After 7 PDH cycles (Fig. 4b), the particles size of PtSn over the PtSn/F-Al_2O_3-Spent is similar to the fresh catalyst, which is determined to be 6.7±2.0 nm. The similar average diameter suggested that the 3D spatial distance of flower-shaped Al_2O_3 structure can efficiently ensure nanoparticles hardly grew and sintered during PDH. Fig. 4c showed that PtSn/C-Al_2O_3-Fresh initially contained particles with the average diameter of 7.0±1.3 nm, which was slightly larger than the particles on PtSn/F-Al_2O_3-Fresh. After

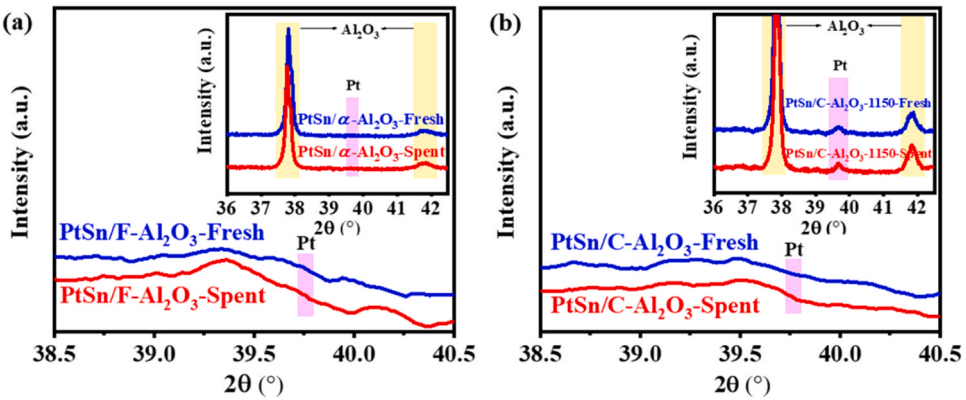

Fig. 3. XRD patterns of the Fresh and Spent (a) PtSn/F-Al_2O_3 and PtSn/α-Al_2O_3; (b) PtSn/C-Al_2O_3 and PtSn/C-Al_2O_3-1150.

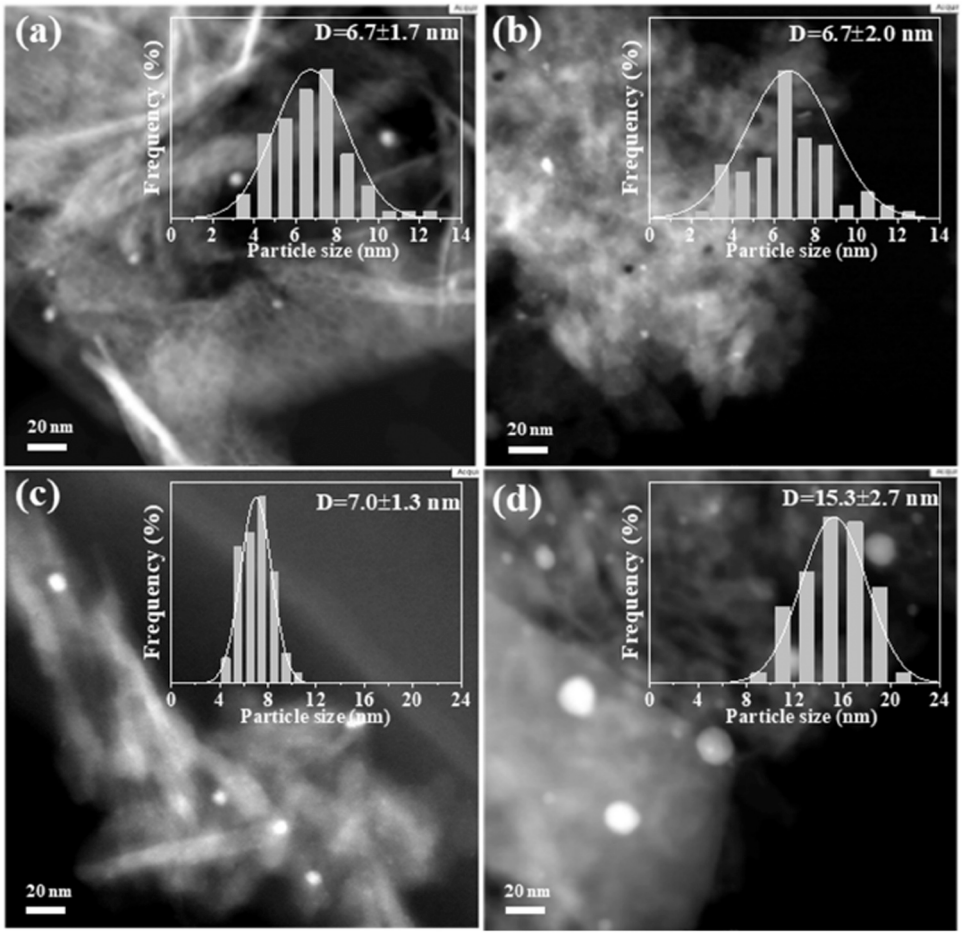

Fig. 4. HAADF-STEM images of PtSn supported on F-Al_2O_3 and C-Al_2O_3 before and PDH and regeneration. (a) PtSn/F-Al_2O_3-Fresh; (b) PtSn/F-Al_2O_3-Spent; (c) PtSn/C-Al_2O_3-Fresh; (d) PtSn/C-Al_2O_3-Spent.

Table 2
The number-averaged diameter of metal nanoparticles determined by STEM.

Catalysts	PtSn/F-Al_2O_3	PtSn/C-Al_2O_3	PtSn/α-Al_2O_3	PtSn/C-Al_2O_3-1150
Fresh	6.7±1.7 nm	7.0±1.3 nm	17.1±4.5 nm	32.0±10.0 nm
Spent	6.7±2.0 nm	15.3±2.7 nm	23.3±6.2 nm	38.0±12.0 nm

7 PDH cycles, PtSn nanoparticles on the PtSn/C-Al_2O_3-Spent grew and sintered into large nanoparticles with the average particle diameter of 15.3±2.3 nm (Fig. 4d). The EDX-Mapping (Fig. S7) of the four catalysts showed that there was no segregation of Pt and Sn after 7 PDH cycles. Fig. S6a-b showed that the average particle diameter of PtSn/α-Al_2O_3 increased from 17.1 to 23.3 nm after 7 PDH cycles, increasing by 36 %. The large nanoparticles on PtSn/α-Al_2O_3-Fresh is due to the low surface area of α-Al_2O_3 support (~6 m^2 g^{-1}), which is similar to the case of C-Al_2O_3-1150 showing the average particle diameter 32.0 nm on PtSn/C-Al_2O_3-1150 and the low surface area of 4 m^2 g^{-1} (Table 1). Based on the statistical results of PtSn particle size, it can be seen intuitively that the unique morphology of flower-shaped Al_2O_3 can effectively inhibit the growth and sintering of metal particles during PDH and regeneration at 600℃, reflecting its superiority on sintering-tolerance in high temperature reactions.

To summarize, the activity results and the *ex-situ* characterizations above indicated that both the PtSn/C-Al_2O_3 and PtSn/α-Al_2O_3 catalysts presented the decrease in conversion after reaction for 6 h and regeneration, corresponding to the increase of average nanoparticle size. The growth of the PtSn nanoparticles on PtSn/C-Al_2O_3 and PtSn/α-Al_2O_3 resulted in irreversible metal sintering and permanent deactivation of catalyst. The α-Al_2O_3 has the spherical structure and the C-Al_2O_3 is nanosheet, whereas the Pt nanoparticles on both supports migrate and sinter during the reaction and regeneration, leading to the permanent deactivation. In contrast, F-Al_2O_3 has the 3D flower-shaped structure and the PtSn/F-Al_2O_3 catalyst presents the deactivation during each run due to coking. The coke can be removed by regeneration to restore to the initial activity after each regeneration. Therefore, the properties and morphology of alumina surface can dramatically affect the deactivation process of catalyst. The flower-shaped Al_2O_3 (F-Al_2O_3) present the 3D structure and the spatial segregation of the nanoparticle prevents the migration and sintering of metal nanoparticles. To reveal the time-resolved evolution of the PtSn particle in the regeneration process (oxidation and reduction), we have further performed the *in-situ* TEM characterization of the catalyst in both oxidative and reductive conditions, as shown below.

3.3. *In-situ characterizations revealing the evolution of Pt species under redox conditions*

3.3.1. *In-situ TEM*

For the *in-situ* characterization, the spent catalysts (after the first run of PDH) were used. The spent PtSn/C-Al_2O_3 and PtSn/F-Al_2O_3 catalysts were treated with O_2 at 500℃ and H_2 at 600℃ in sequence to simulate the removal of coke under oxidative atmosphere and the PDH reaction under reductive atmosphere. At the same time, the evolution of particle size was directly observed by *in-situ* TEM and the results are shown in Fig. 5, Fig. 6 and Fig. S8.

For the spent PtSn/C-Al_2O_3 catalyst after the first PDH run, to

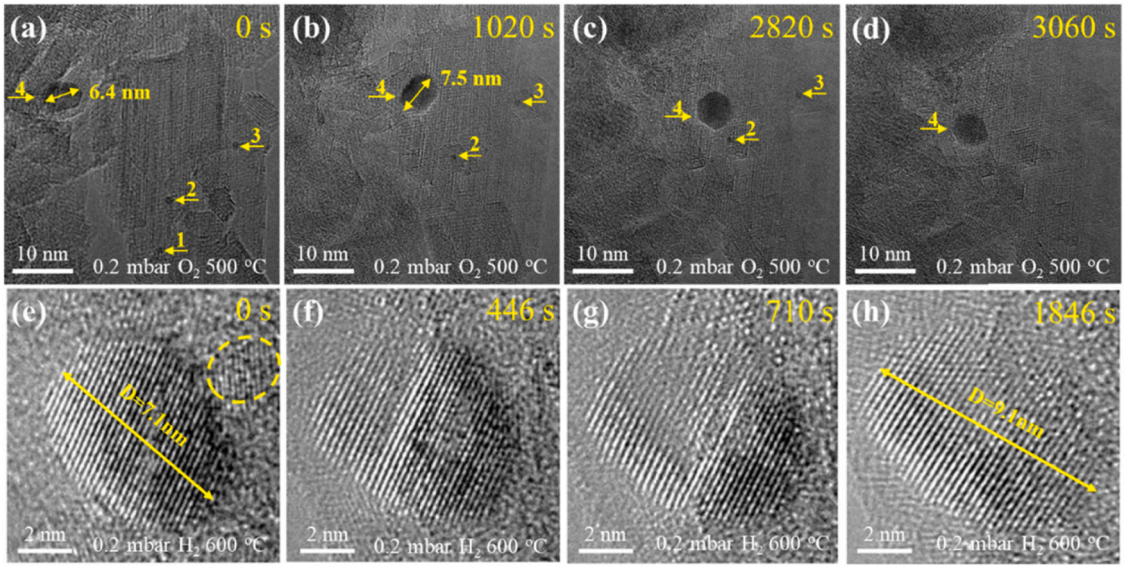

Fig. 5. Time-resolved evolution of PtSn/C-Al_2O_3 nanoparticle under redox conditions at elevated temperatures. (a-d) 500°C in O_2 (0.2 mbar); (e-h) 600°C in H_2 (0.2 mbar).

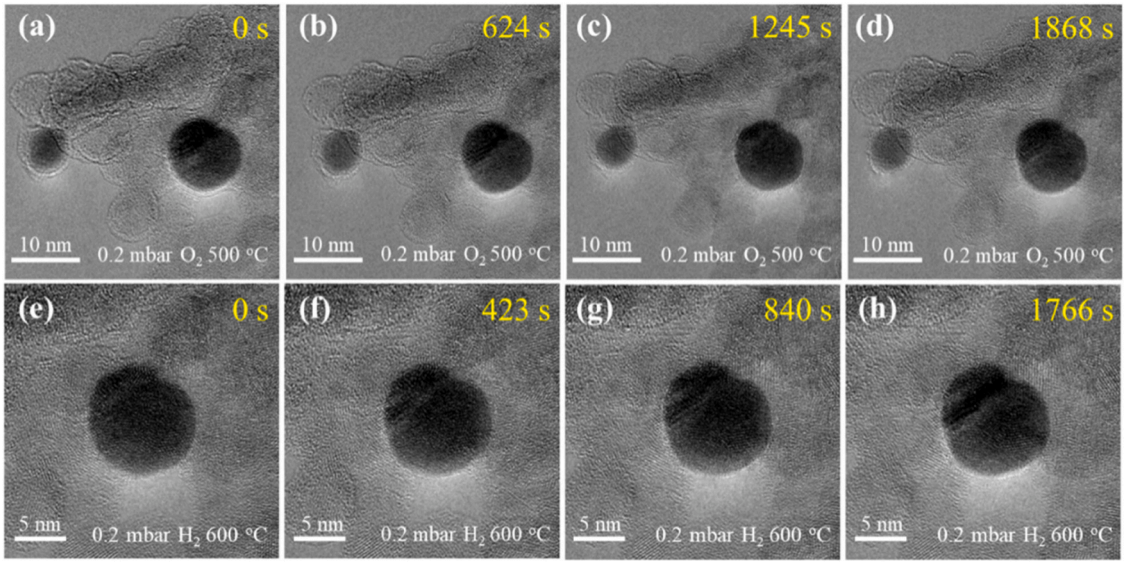

Fig. 6. Time-resolved evolution of PtSn/F-Al_2O_3 nanoparticle under redox conditions at elevated temperatures. (a-d) 500°C in O_2 (0.2 mbar); (e-h) 600°C in H_2 (0.2 mbar).

simulate the oxidation process in the regeneration, a flowing O_2 gas (99.999 %) at the pressure of 0.2 mbar was introduced into the *in-situ* TEM chamber through a variable pressure leak valve and then the temperature of the heating area of the chip was raised to 500 °C at a rate of 10 °C/s. The time-resolved images were collected and are shown in Fig. 5a-d. From the *in-situ* TEM (Fig. 5a-d), it can be observed that under 0.2 mbar O_2 and 500°C, the size of the nanoparticle 4 (with a length of 6.4 nm) increased to 7.5 nm. At the same time, nanoparticle 1 disappeared, and the size of the particles 2 and 3 decreased. This indicates that under oxygen and high-temperature conditions, particle growth follows the Ostwald ripening (OR) mechanism. We also observed changes in the position of nanoparticle 4 over time, as well as the migration and fusion of small nanoparticles with large ones (see Supplementary Video 1). Moreover, to mitigate the effects of electron beam, we minimized the beam intensity. Under the conditions of Beam Blanking where the electron beam only irradiates the sample during image acquisition, we collected a series of *in-situ* TEM images showing the growth of nanoparticles in oxidizing conditions (Fig. S8a-d). Under high-temperature and oxygen atmosphere conditions, nanoparticles 1 and 2 eventually merged into a larger particle (labeled as particle 3). Meanwhile, over time, particle 4 continued to grow. Therefore, particle migration and coalescence (PMC) was also observed, confirming that particle growth is not caused by electron beam effects. In summary, under oxygen and high-temperature conditions, we observed the disappearance of small particles, enlargement of large particles, and sintering caused by particle migration via *in-situ* TEM. This demonstrates that both OR and PMC mechanisms coexist during particle growth.

After the removal of coke, the O_2 was evacuated from the electron microscope chamber and switched to H_2 at the pressure of 0.2 mbar and T = 600 ℃. Fig. 5e-h showed the TEM images of the size evolution with time that the size of the nanoparticle increased from 7.1 to 9.1 nm and the small nanoparticle surrounding disappeared after 1846 s Fig. S8e-h also showed that two adjacent small metal nanoparticles completely fused into one large metal nanoparticle after 174 s. At low

magnification, many small metal nanoparticles disappeared and became large nanoparticles after 515 s (Fig. S8i-l). Moreover, we also observed the migration and coalescence of nanoparticles under high-temperature and 0.2 mbar H_2 conditions (see Supplementary Video 2). The *in-situ* TEM results above showed obvious phenomenon of metal nanoparticles ripening, and also indicated that the nanoparticles of PtSn/C-Al_2O_3 sintered and grew under PDH reaction condition. In contrast, for PtSn/F-Al_2O_3, there was no change in the diameter of nanoparticles (Fig. 6) after exposing either in O_2 for 1866 s (Fig. 6a-d) or in H_2 for 1816 s (Fig. 6e-h), which is consistent with the results of *ex-situ* TEM that there was no change for the average particle size of PtSn/F-Al_2O_3 after 7 cycles PDH. Therefore, combining the results obtained from both the *in-situ* and *ex-situ* TEM results, it concludes that the nanoparticles on PtSn/C-Al_2O_3 sintered under both oxidative and reductive atmospheres. On the contrary, the nanoparticles on PtSn/F-Al_2O_3 do not sinter under both oxidative and reductive atmospheres. The results of *in-situ* electron microscopy directly confirmed the effectiveness of the compartmentalized strategy by constructing a 3D spatial distance, and the flower-shaped Al_2O_3 can effectively prevent the migration and growth of metal nanoparticles at high temperature.

Supplementary material related to this article can be found online at doi:10.1016/j.apcatb.2024.124334.

3.3.2. *In-situ CO-DRIFTS*

We also used *in-situ* CO-DRIFTS to investigate the effect of the alumina morphology on the sintering behavior of the Pt species over different catalysts before and after 7 PDH cycles. Fig. 7 presented the DRIFTS spectra of CO adsorption on PtSn/F-Al_2O_3 and PtSn/C-Al_2O_3 before and after reaction and regeneration. Two bands centered at 2069 and 2056 cm^{-1} attributing to linearly adsorbed CO on Pt nanoparticles [38–40] were observed on PtSn/F-Al_2O_3-Fresh (Fig. 7a). Moreover, there is no bridge-adsorbed CO on PtSn nanoparticles. After the removal of coke on the spent catalyst after PDH, the CO band shifted from 2069 to 2048 cm^{-1} due to the lower CO coverage on the spent catalyst (PtSn/F-Al_2O_3-O). After the reduction, the band intensity at 2048 cm^{-1} weakened and further shifted to 2037 cm^{-1} (PtSn/F-Al_2O_3-O-R). The shift to lower wavenumber may indicate that the electron density of Pt species became higher after reduction, possibly due to the effect of Sn promoter, in which Sn transferred electrons to Pt species during PDH cycles. The enhanced electron density of Pt can weaken the adsorption of propylene, thus reducing the occurrence of side reactions and the formation of coke. Two bands at 2069 and 2052 cm^{-1} attributing to linearly adsorbed CO on Pt nanoparticles, were also observed over the PtSn/C-Al_2O_3-Fresh catalyst (Fig. 7b). The band at 1836 cm^{-1} is attributed to the bridge-adsorbed CO on Pt nanoparticles. After the removal of coke on the spent catalyst during regeneration (PtSn/C-Al_2O_3-O), the bridge CO disappeared, and the linear CO band shifted from 2069 to 2052 cm^{-1}, which also showing the low intensity (Fig. 7b), indicating the low Pt dispersion (*i.e.* large Pt size due to sintering). After H_2 reduction (PtSn/C-Al_2O_3-O-R), the band at 2052 cm^{-1} disappeared completely, which is due to the surface reconstruction of Pt particles caused by regeneration, possibly demonstrating the severe sintering of Pt particles. The CO band disappeared completely on the catalyst supported on C-alumina and diminished significantly on that supported on the F-alumina after regeneration. Since several cycles of oxidation and reduction were conducted prior to the DRIFTS of the spent catalyst, it is assumed that the oxidation/reduction process affected the shape or surface composition of the particles or caused the surface restructure, leading to the different CO adsorption behavior.

3.4. *Computational study*

To elucidate the impact of Al_2O_3 support morphology on the stability of PtSn/Al_2O_3 catalysts, we conducted a series of computational investigations. Under realistic reaction conditions, the sintering of metal nanoparticles primarily occurs through particle migration and coalescence (PMC) and Ostwald ripening (OR) mechanisms. In this study, we obtained the contact angle of PtSn nanoparticles using molecular dynamics simulations, from which we derived the particles' diffusion coefficients and their diffusion lengths over a period of time. By comparing the differences in morphology between the F-Al_2O_3 and C-Al_2O_3 supports and their effects on sintering, we can explain the different sintering behaviors of the nanoparticles on F-Al_2O_3 and C-Al_2O_3 supports.

The rate of PMC process is fundamentally determined by the diffusion coefficient $D_p(R)$ of particles on the support surface, as established in our earlier work [41,42]. As shown in Eq. 1, $D_p(R)$ is influenced by metal's composition reflected by metal atom's self-activation energy E^m_{act} that characterizes the formation and migration of atoms on the nanoparticle surface, which is evidenced as one-third of the cohesive energy of bulk PtSn alloy(see more details in Fig. S11) [41]. The spatial distribution of the particles also significantly affect the PMC kinetics as proved [43], further leading to the modulation of critical loading of supported nanoparticles as revealed in the following [44].

$$D_p(R) = \frac{K_\alpha}{R^4}\exp\left[\frac{\Delta\mu(R)}{k_B T}\right]\exp\left[-\frac{E^m_{act} - S^m E_{adh}}{k_B T}\right] \quad (1)$$

where, R represents the radius of curvature of the supported particle. K_α denotes the structure factor associated with the contact angle α between the metal particle and the support. k_B stands for Boltzmann's constant. T represent temperature. S^m is the average area of the Pt and Sn atom in PtSn nanoparticles (8.23 $Å^2$) [45]. $\Delta\mu(R)$ stands for the chemical potential of the metal atoms within supported nanoparticles relative to their bulk counterparts, which is approximately represented as using the Gibbs-Thomson (G-T) relations:

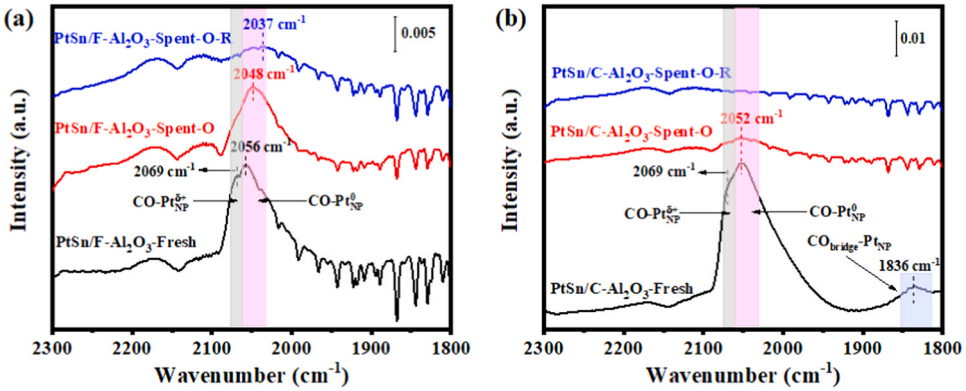

Fig. 7. *In-situ* DRIFTS spectra of CO adsorption over Fresh and Spent (a) PtSn/F-Al_2O_3 and (b) PtSn/C- Al_2O_3. ("O" represents "Oxidation for the removal of coke" and "R" represents "Reduction").

$$\Delta\mu(R) = \frac{2\Omega\gamma_m(R)}{R} \quad (2)$$

where, $\gamma_m(R)$ represents the surface energy of PtSn nanoparticles, whose dependence on the size due to the increase in low coordination sites which has been fitted in the Supplementary Fig. S10. Ω represents the average volume of Pt and Sn atoms within PtSn nanoparticles, which is measured to be 23.61 Å^3 [45]. For a metal nanoparticle with a given volume V_0, when it comes into contact with support, it tends to form a hemispherical shape particle that can be characterized by the parameter α_1. The value of α_1, in turn, determines the corresponding radius R:

$$R = \left(\frac{3V_0}{4\pi\alpha_1}\right)^{1/3} \quad (3)$$

where,

$$\alpha_1 = \frac{[2 - 3\cos(\alpha) + \cos^3(\alpha)]}{4} \quad (4)$$

Another important factor is the adhesive effect of the support on the metal, whose effects on the sintering kinetics have been systematically and quantitatively described in our theoretical model [42,46]. The adhesive effect of the support can be quantified by the adhesion energy (E_{adh}) between nanoparticles and the support [45], which is closely related to α according to the Young-Dupre' equation:

$$E_{adh} = -\gamma_m(1 + \cos\alpha) \quad (5)$$

For a period of time τ, the spatial dimension of the PtSn nanoparticle diffusion *via* Brownian motion can be measured by a characteristic diffusion length L:

$$L = [D_p(\alpha)\tau]^{1/2} \quad (6)$$

Assuming the support with an area of $\pi(L/2)^2$ only supports one particle, the critical loading of the supported Pt nanoparticles with a volume of $4\pi\alpha_1 R^3/3$ can be estimated by :

$$\text{Loading} = \frac{16 S_m R^3 \alpha_1 m}{3L^2\Omega} \quad (7)$$

where, S_m is a given mass specific surface area of the support, m is the average atom mass (2.32×10^{-22} g/atom).

Consequently, to calculate the diffusion coefficient and thereby the critical loading of supported PtSn nanoparticles on Al_2O_3 support in a certain temperature, we need to calculate α on the support. To achieve it, molecular dynamic (MD) simulations based on first-principles neural network potential were performed to obtain the trajectory of particle motion, which can be used to analyze the contact angle of metal nanoparticles on the support. Based on previous research, the (100) and (110) surfaces of γ-Al_2O_3 are identified as the most stable surfaces exposed [47]. In this study, we constructed a pristine $5\times5\times1$ γ-Al_2O_3(100) surface with 30 angstrom vacuum layer model to simulate the commercial Al_2O_3 nanosheet. A $Pt_{18}Sn_{46}$ metal nanoparticle (ratio of Pt to Sn is 1:2.5) was loaded on the support. The NVT ensemble were used in all the MD simulations. The simulated temperature was held at 873 K and controlled by a Nosé-Hoover thermostat and all atoms in Al_2O_3 support are fixed in simulation. The MD simulation was equilibrated for 100 ps, followed by a 200 ps production run to obtain the geometric shape of PtSn nanoparticles on the support during their movement. The MD simulation were performed in LASP code [36]. The geometric shape of the supported PtSn nanoparticles was characterized by enclosing them within the Minimum Bounding Sphere, based on the structure observed in hundreds of frames following equilibrium in the MD simulation (see Fig. S9), we found that α of PtSn nanoparticles is 102.1°for C-Al_2O_3. Based on the extracted α and in terms of the size effect on γ_m, the $\Delta\mu$ of PtSn nanoparticles on the support was calculated and plotted with the particle size in Fig. 8a. We then calculated D_p of PtSn nanoparticles versus the particle size on different Al_2O_3 supports at 600 ℃, as shown in Fig. 8b. For 3.2 nm PtSn nanoparticles, the calculated D_p is 0.34 nm^2/s on C-Al_2O_3. During 7 PDH cycles, the critical loading for a C-Al_2O_3 support with a specific surface area of 106 g/m^2 was 1.7 % wt. This value represents the maximum metal loading at which metal nanoparticles do not undergo severe sintering under the PMC mechanism, which is very close to the metal loading used in experiments (0.5 wt% of Pt and 0.8 wt% of Sn). Due to the simultaneous presence of the OR process during sintering, severe sintering occurred with the metal nanoparticles on the C-Al_2O_3 support.

For the F-Al_2O_3 support, which has a similar specific surface area to the C-Al_2O_3, the spatial compartmentalizing effects completely restrict the diffusion of aged monomers during the OR process, thereby blocking the ripening process. Additionally, for the PMC process, this spatial segregation increases the diffusion length required for the coalescence of two nanoparticles, which in turn slows down the sintering process associated with PMC. In summary, this spatial segregation increases the difficulty of both the PMC and OR processes, thereby improving the F-Al_2O_3 support's sintering resistance.

4. Conclusion

Metal catalysts deactivate in propane dehydrogenation (PDH) due to the formation of coking or nanoparticle sintering. The deactivated catalysts can be regenerated by treatments involving oxidation and reduction. However, the dynamic evolution of the catalyst during the regeneration is unknown. In this study, *via in-situ* and *ex-situ* TEM characterizations, we found that the PtSn nanoparticles on two-dimensional alumina (PtSn/C-Al_2O_3) sintered under both oxidative and reductive atmospheres, leading to the permanent deactivation in PDH, which was carried out by cofeeding H_2 and the absence of steam. The average particle diameter of nanoparticles increased from 7.0 nm to

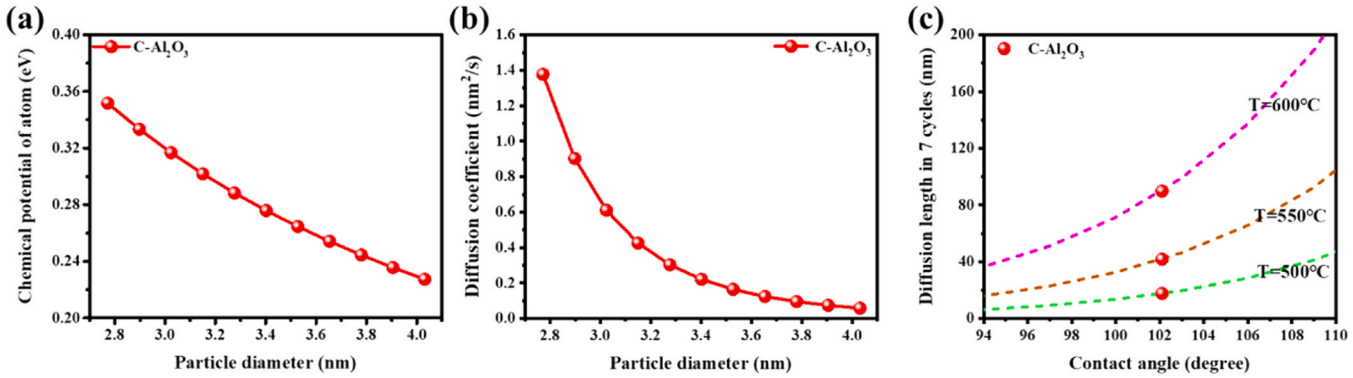

Fig. 8. (a) Size dependence of atomic chemical potential in PtSn nanoparticles and (b) diffusion coefficient of PtSn nanoparticles on the C-Al_2O_3 support. (c) Calculated diffusion length of PtSn nanoparticles in 42 h (7 PDH cycles) versus the contact angles of PtSn nanoparticles under different temperatures.

15.3 nm after 7 PDH cycles. After 6 h reaction for each recycle, the conversion of propane decreased from 40.0 % to 17.0 %. By designing a 3D flower-shaped Al_2O_3 (F-Al_2O_3), the metal nanoparticles were stabilized through a compartmentalization strategy by constructing spatial distances. The synthesized PtSn/F-Al_2O_3 catalyst does not sinter under both high-temperature oxidative and reductive atmospheres during regeneration, demonstrating the stable reactivity in PDH. Theoretical studies revealed the mechanism of stabilizing metal nanoparticles with three-dimensional support. The facial strategy of using 3D spatial segregation to stabilize metal nanoparticles potentially provided a route for designing stable metal nanocatalysts suitable for high temperature reactions.

CRediT authorship contribution statement

Wei Xue Li: Funding acquisition, Project administration, Software. **Haifeng Xiong:** Writing – review & editing, Writing – original draft, Supervision, Funding acquisition, Formal analysis, Conceptualization. **Sulei Hu:** Writing – review & editing, Supervision, Formal analysis, Conceptualization. **Jianyu Huang:** Visualization, Investigation. **Fan Yang:** Resources, Formal analysis. **Jianyu Hu:** Software. **Haowen Li:** Writing – review & editing, Writing – original draft, Data curation. **Congcong Du:** Writing – original draft, Data curation. **Zhun Zhang:** Writing – review & editing, Writing – original draft, Investigation, Data curation, Conceptualization.

Declaration of Competing Interest

The authors declare that they have no known competing financial interests or personal relationships that could have appeared to influence the work reported in this paper.

Data availability

Data will be made available on request.

Acknowledgements

The work was financially supported by the National Key R&D Program of China (2021YFB3502000), the National High-Level Talent Fund and the National Natural Science Foundation of China (Grant No. 22072118, 22221003, 22173058, 22372153 and 22372138), National Program for Support of Top-notch Young Professional, Chinese Academy of Sciences Youth Innovation Promotion Association, the Strategic Priority Research Program of the Chinese Academy of Sciences (XDB0450102), Innovation Program for Quantum Science and Technology (2021ZD0303302), K. C. Wong Education (GJTD-2020-15), Anhui Outstanding Youth Fund (2208085J27), the Fundamental Research Funds for the Central Universities (20720220009). The authors also thank financial support from the State Key Laboratory of Physical Chemistry of Solid Surfaces of Xiamen University, Supercomputing Center of University of Science and Technology of China and Hefei Advanced Computing Center. National Natural Science Foundation of China (Nos. U20A20336, 21935009), Natural Science Foundation of Hebei Province (No. B2020203037), are also acknowleged for financial support of this research.

Appendix A. Supporting information

The details of catalytic performance (Fig. S1, Long-term stability test for PtSn/F-Al_2O_3; Fig. S2, Catalytic performances of PtSn/C-Al_2O_3-1150), characterizations of catalysts (Fig. S3-Fig. S8) and theoretical studies (Fig. S9-Fig. S11) are summarized in supporting information. Supplementary data associated with this article can be found in the online version at doi:10.1016/j.apcatb.2024.124334.

References

[1] Z. Hu, D. Yang, Z. Wang, Z. Yuan, State-of-the-art catalysts for direct dehydrogenation of propane to propylene, Chin. J. Catal. 40 (2019) 1233–1254.
[2] S. Chen, X. Chang, G. Sun, T. Zhang, Y. Xu, Y. Wang, C. Pei, J. Gong, Propane dehydrogenation: catalyst development, new chemistry, and emerging technologies, Chem. Soc. Rev. 50 (2021) 3315–3354.
[3] Y. Dai, X. Gao, Q. Wang, X. Wan, C. Zhou, Y. Yang, Recent progress in heterogeneous metal and metal oxide catalysts for direct dehydrogenation of ethane and propane, Chem. Soc. Rev. 50 (2021) 5590–5630.
[4] J. Wu, G. Zhao, M. Song, H. Wang, Y. Wei, X. Chen, G. Wang, Z. Yan, Nanosheets-stacked Al_2O_3-flower anchoring Pt catalyst for intensified ethylene production from ethane dehydrogenation, Fuel 329 (2022) 125381.
[5] L. Shi, G. Deng, W. Li, S. Miao, Q. Wang, W. Zhang, A. Lu, Al_2O_3 nanosheets rich in pentacoordinate Al^{3+} ions stabilize Pt-Sn clusters for propane dehydrogenation, Angew. Chem. Int. Ed. 54 (2015) 13994–13998.
[6] Y. Pan, A. Bhowmick, W. Wu, Y. Zhang, Y. Diao, A. Zheng, C. Zhang, R. Xie, Z. Liu, J. Meng, D. Liu, Titanium silicalite-1 nanosheet-supported platinum for non-oxidative ethane dehydrogenation, ACS Catal. 11 (2021) 9970–9985.
[7] Q. Sun, N. Wang, Q. Fan, L. Zeng, A. Mayoral, S. Miao, R. Yang, Z. Jiang, W. Zhou, J. Zhang, T. Zhang, J. Xu, P. Zhang, J. Cheng, D.C. Yang, R. Jia, L. Li, Q. Zhang, Y. Wang, O. Terasaki, J. Yu, Subnanometer bimetallic platinum-zinc clusters in zeolites for propane dehydrogenation, Angew. Chem. Int. Ed. 59 (2020) 2–11.
[8] J. Zhu, R. Osuga, R. Ishikawa, N. Shibata, Y. Ikuhara, J.N. Kondo, M. Ogura, J. Yu, T. Wakihara, Z. Liu, T. Okubo, Ultrafast encapsulation of metal nanoclusters into mfi zeolite in the course of its crystallization: catalytic application for propane dehydrogenation, Angew. Chem. Int. Ed. 59 (2020) 1–7.
[9] H. Wang, L. Sun, Z. Sui, Y. Zhu, G. Ye, D. Chen, X. Zhou, W. Yuan, Coke formation on Pt–Sn/Al_2O_3 catalyst for propane dehydrogenation, Ind. Eng. Chem. Res. 57 (2018) 8647–8654.
[10] P.N. Plessow, F. Abild-Pedersen, Sintering of Pt nanoparticles via volatile PtO_2: simulation and comparison with experiments, ACS Catal. 6 (2016) 7098–7108.
[11] M.A. Ha, E.T. Baxter, A.C. Cass, S.L. Anderson, A.N. Alexandrova, Boron switch for selectivity of catalytic dehydrogenation on size-selected Pt clusters on Al_2O_3, J. Am. Chem. Soc. 139 (2017) 11568–11575.
[12] J. Dadras, E. Jimenez-Izal, A.N. Alexandrova, Alloying Pt sub-nano-clusters with boron: sintering preventative and coke antagonist? ACS Catal. 5 (2015) 5719–5727.
[13] H. Zhu, D.H. Anjum, Q. Wang, E. Abou-Hamad, L. Emsley, H. Dong, P. Laveille, L. Li, A.K. Samal, J.-M. Basset, Sn surface-enriched Pt–Sn bimetallic nanoparticles as a selective and stable catalyst for propane dehydrogenation, J. Catal. 320 (2014) 52–62.
[14] L. Liu, M. Lopez-Haro, C.W. Lopes, S. Rojas-Buzo, P. Concepcion, R. Manzorro, L. Simonelli, A. Sattler, P. Serna, J.J. Calvino, A. Corma, Structural modulation and direct measurement of subnanometric bimetallic PtSn clusters confined in zeolites, Nat. Catal. 3 (2020) 628–638.
[15] L. Liu, M. Lopez-Haro, C.W. Lopes, C. Li, P. Concepcion, L. Simonelli, J.J. Calvino, A. Corma, Regioselective generation and reactivity control of subnanometric platinum clusters in zeolites for high-temperature catalysis, Nat. Mater. 18 (2019) 866–873.
[16] Y. Zhou, F. Wei, H. Qi, Y. Chai, L. Cao, J. Lin, Q. Wan, X. Liu, Y. Xing, S. Lin, A. Wang, X. Wang, T. Zhang, Peripheral-nitrogen effects on the Ru_1 centre for highly efficient propane dehydrogenation, Nat. Catal. 5 (2022) 1145–1156.
[17] W. Wang, S. Chen, C. Pei, R. Luo, J. Sun, H. Song, G. Sun, X. Wang, Z. Zhao, J. Gong, Tandem propane dehydrogenation and surface oxidation catalysts for selective propylene synthesis, Science 381 (2023) 886–890.
[18] H. Xiong, S. Lin, J. Goetze, P. Pletcher, H. Guo, L. Kovarik, K. Artyushkova, B. M. Weckhuysen, A.K. Datye, Thermally stable and regenerable platinum–tin clusters for propane dehydrogenation prepared by atom trapping on Ceria, Angew. Chem. Int. Ed. 56 (2017) 8986–8991.
[19] H.N. Pham, J.J. Sattler, B.M. Weckhuysen, A.K. Datye, Role of Sn in the regeneration of Pt/γ-Al_2O3 light alkane dehydrogenation catalysts, ACS Catal. 6 (2016) 2257–2264.
[20] J. Zhu, M. Yang, Y. Yu, Y. Zhu, Z. Sui, X. Zhou, A. Holmen, D. Chen, Size-dependent reaction mechanism and kinetics for propane dehydrogenation over Pt catalysts, ACS Catal. 5 (2015) 6310–6319.
[21] T.W. HANSEN, A.T. DELARIVA, S.R. CHALLA, A.K. DATYE, Sintering of catalytic nanoparticles: particle migration or Ostwald ripening? Acc. Chem. Res. 46 (2013) 1720–1730.
[22] P. Tabib Zadeh Adibi, T. Pingel, E. Olsson, H. Grönbeck, C. Langhammer, Pt nanoparticle sintering and redispersion on a heterogeneous nanostructured support, J. Phys. Chem. C 120 (2016) 14918–14925.
[23] S.B. Simonsen, I. Chorkendorff, S. Dahl, M. Skoglundh, J. Sehested, S. Helveg, Direct observations of oxygen-induced platinum nanoparticle ripening studied by in situ TEM, J. Am. Chem. Soc. 132 (2010) 7968–7975.
[24] L. Liu, D.N. Zakharov, R. Arenal, P. Concepcion, E.A. Stach, A. Corma, Evolution and stabilization of subnanometric metal species in confined space by in situ TEM, Nat. Commun. 9 (2018) 574.
[25] P. Wang, J. Yao, Q. Jiang, X. Gao, D. Lin, H. Yang, L. Wu, Y. Tang, L. Tan, Stabilizing the isolated Pt sites on PtGa/Al_2O_3 catalyst via silica coating layers for propane dehydrogenation at low temperature, Appl. Catal. B Environ. 300 (2022) 120731.
[26] Y. Gu, H. Liu, M. Yang, Z. Ma, L. Zhao, W. Xing, P. Wu, X. Liu, S. Mintova, P. Bai, Z. Yan, Highly stable phosphine modified VOx/Al_2O_3 catalyst in propane dehydrogenation, Appl. Catal. B Environ. 274 (2020) 119089.

[27] Y. Chai, S. Chen, Y. Chen, F. Wei, L. Cao, J. Lin, L. Li, X. Liu, S. Lin, X. Wang, T. Zhang, Dual-atom catalyst with N-colligated Zn_1Co_1 species as dominant active sites for propane dehydrogenation, J. Am. Chem. Soc. 146 (2024) 263–273.
[28] G. Sun, Z. Zhao, R. Mu, S. Zha, L. Li, S. Chen, L. Zeng, J. Gong, G. Sun, Z. Zhao, R. Mu, S. Zha, L. Li, S. Chen, L. Zeng, J. Gong, K. Zang, J. Luo, Z. Li, S.C. Purdy, J. T. Miller, A.J. Kropf, J.T. Miller, L. Zeng, J. Gong, Breaking the scaling relationship via thermally stable Pt/Cu single atom alloys for catalytic dehydrogenation, Nat. Commun. 9 (2018) 4454.
[29] Y. Nakaya, J. Hirayama, S. Yamazoe, K.I. Shimizu, S. Furukawa, Single-atom Pt in intermetallics as an ultrastable and selective catalyst for propane dehydrogenation, Nat. Commun. 11 (2020) 2838.
[30] N. Kong, X. Fan, F. Liu, L. Wang, H. Lin, Y. Li, S.T. Lee, Single vanadium atoms anchored on graphitic carbon nitride as a high-performance catalyst for non-oxidative propane dehydrogenation, ACS Nano 14 (2020) 5772–5779.
[31] Y. Nakaya, E. Hayashida, H. Asakura, S. Takakusagi, S. Yasumura, K.I. Shimizu, S. Furukawa, High-entropy intermetallics serve ultrastable single-atom Pt for propane dehydrogenation, J. Am. Chem. Soc. 144 (2022) 15944–15953.
[32] Y. Wang, Z. Hu, X. Lv, L. Chen, Z. Yuan, Ultrasmall PtZn bimetallic nanoclusters encapsulated in silicalite-1 zeolite with superior performance for propane dehydrogenation, J. Catal. 385 (2020) 61–69.
[33] T. Wang, F. Jiang, G. Liu, L. Zeng, Z. Zhao, J. Gong, Effects of Ga doping on Pt/CeO_2-Al_2O_3 catalysts for propane dehydrogenation, AlChE J. 62 (2016) 4365–4376.
[34] J.J. Sattler, I.D. Gonzalez-Jimenez, L. Luo, B.A. Stears, A. Malek, D.G. Barton, B. A. Kilos, M.P. Kaminsky, T.W. Verhoeven, E.J. Koers, M. Baldus, B.M. Weckhuysen, Platinum-promoted Ga/Al_2O_3 as highly active, selective, and stable catalyst for the dehydrogenation of propane, Angew. Chem. Int. Ed. 53 (2014) 9251–9256.
[35] X. Yang, Q. Li, E. Lu, Z. Wang, X. Gong, Z. Yu, Y. Guo, L. Wang, Y. Guo, W. Zhan, J. Zhang, S. Dai, Taming the stability of Pd active phases through a compartmentalizing strategy toward nanostructured catalyst supports, Nat. Commun. 10 (2019) 1611.
[36] S.D. Huang, C. Shang, P.L. Kang, X.J. Zhang, Z.P. Liu, LASP: fast global potential energy surface exploration, WIREs Comput. Mol. Sci. 9 (2019) e1415.
[37] G. Kresse, J. Furthmiiller, Efficiency of ab-initio total energy calculations for metals and semiconductors using a plane-wave basis set, Comput. Mater. Sci. 6 (1996) 15–50.
[38] C. Wang, X.-K. Gu, H. Yan, Y. Lin, J. Li, D. Liu, W.-X. Li, J. Lu, Water-mediated mars–van krevelen mechanism for CO oxidation on CeriA-supported Single-atom Pt_1 catalyst, ACS Catal. 7 (2017) 887–891.
[39] L. DeRita, S. Dai, K. Lopez-Zepeda, N. Pham, G.W. Graham, X. Pan, P. Christopher, Catalyst architecture for stable single atom dispersion enables site-specific spectroscopic and reactivity measurements of CO adsorbed to Pt atoms, oxidized Pt clusters, and metallic Pt clusters on TiO_2, J. Am. Chem. Soc. 139 (2017) 14150–14165.
[40] I.M.C. Curators, N. Del-Toro, M. Duesbury, M. Koch, L. Perfetto, A. Shrivastava, D. Ochoa, O. Wagih, J. Pinero, M. Kotlyar, C. Pastrello, P. Beltrao, L.I. Furlong, I. Jurisica, H. Hermjakob, S. Orchard, P. Porras, Capturing variation impact on molecular interactions in the IMEx Consortium mutations data set, Nat. Commun. 10 (2019) 10.
[41] S. Hu, W. Li, Sabatier principle of metal-support interaction for design of ultrastable metal nanocatalysts, Science 374 (2021) 1360–1365.
[42] S. Hu, W. Li, Metal-support interaction controlled migration and coalescence of supported particles, Sci. China Technol. Sci. 62 (2019) 762–772.
[43] S. Hu, W. Li, Influence of particle size distribution on lifetime and thermal stability of ostwald ripening of supported particles, ChemCatChem 10 (2018) 2900–2907.
[44] P. Yin, S. Hu, K. Qian, Z. Wei, L. Zhang, Y. Lin, W. Huang, H. Xiong, W. Li, H. Liang, Quantification of critical particle distance for mitigating catalyst sintering, Nat. Commun. 12 (2021) 4865.
[45] C.T. Campbell, J.R.V. Sellers, Anchored metal nanoparticles: effects of support and size on their energy, sintering resistance and reactivity, Faraday Discuss. 162 (2013) 9–30.
[46] S. Hu, W. Li, Theoretical investigation of metal-support interactions on ripening kinetics of supported particles, ChemNanoMat 4 (2018) 510–517.
[47] M. Digne, P. Sautet, P. Raybaud, P. Euzen, H. Toulhoat, Hydroxyl groups on γ-alumina surfaces: a DFT study, J. Catal. 211 (2002) 1–5.